

Manuscript version: Author's Accepted Manuscript

The version presented in WRAP is the author's accepted manuscript and may differ from the published version or Version of Record.

Persistent WRAP URL:

<http://wrap.warwick.ac.uk/163017>

How to cite:

Please refer to published version for the most recent bibliographic citation information.

Copyright and reuse:

The Warwick Research Archive Portal (WRAP) makes this work by researchers of the University of Warwick available open access under the following conditions.

Copyright © and all moral rights to the version of the paper presented here belong to the individual author(s) and/or other copyright owners. To the extent reasonable and practicable the material made available in WRAP has been checked for eligibility before being made available.

Copies of full items can be used for personal research or study, educational, or not-for-profit purposes without prior permission or charge. Provided that the authors, title and full bibliographic details are credited, a hyperlink and/or URL is given for the original metadata page and the content is not changed in any way.

Publisher's statement:

Please refer to the repository item page, publisher's statement section, for further information.

For more information, please contact the WRAP Team at: wrap@warwick.ac.uk.

Ferroelectric incommensurate spin crystal

Dorin Rusu¹, Jonathan J. P. Peters^{1,2}, Thomas P. A. Hase¹, James A Gott¹, Gareth A. A. Nisbet³, Jörg Strempler⁴, Daniel Haskel⁴, Samuel D. Seddon¹, Richard Beanland¹, Ana M. Sanchez¹ and Marin Alexe¹

¹*Department of Physics, University of Warwick, Coventry, CV4 7AL, United Kingdom*

²*School of Physics, Trinity College Dublin, Dublin, Ireland*

³*Diamond Light Source, Didcot, OX11 0DE, United Kingdom*

⁴*Argonne National Laboratory, Lemont, IL 60439, United States of America*

Ferroics, especially ferromagnets, can form complex topological spin structures such as vortices¹ and skyrmions^{2, 3}, when subjected to particular electrical and mechanical boundary conditions. Simple vortex-like electric dipole-based topological structures have been observed in dedicated ferroelectric systems, especially ferroelectric/insulator superlattices, such as $\text{PbTiO}_3/\text{SrTiO}_3$ that have proven to be an ideal environment due to high depolarising field⁴⁻¹². As of yet, the electric dipole equivalent of ordered magnetic spin lattices driven by the Dzyaloshinskii–Moriya interaction (DMI)^{13, 14} has not been experimentally observed. Here we examine a novel domain structure in single PbTiO_3 epitaxial layer sandwiched between SrRuO_3 electrodes. We observe periodic clockwise and anti-clockwise ferroelectric vortices which are modulated by a second ordering along their toroidal core. The result, supported by calculations, is a labyrinth-like pattern with two orthogonal periodic modulations which form an incommensurate polar crystal, that provides a ferroelectric analogue to the recently discovered incommensurate spin crystals in ferromagnetic materials¹⁵⁻¹⁷. These findings further blur the border between emergent ferromagnetic and ferroelectric topologies, clearing the way for experimental realisation of further electric counterparts of magnetic DMI driven phases.

Despite the fundamental difference in the origin and strengths of internal magnetic and electric fields, similar dipolar topologies manifest in both ferroelectrics and ferromagnets. The current understanding of what drives these topologies is based on the complex interplay between strain, electric and polarization gradient energies¹⁸. For example, polar vortices have been discovered in thin ferroelectric films and extensively studied in an environment which maximizes the depolarization field generated by the surface charges in ferroelectric-insulator superlattices^{7, 8, 19-21}. The use of insulating layers hinders the integration of such heterostructures into devices that could make use of the electronic characteristics of the complex topologies^{22, 23}. However, ferroelectric heterostructures with metallic contacts, which are significantly easier to incorporate into technological devices, have to date been shown only to stabilize more common

topologies, such as 180° domains with localized polar vortices at the domain walls²⁴ or flux-closure type domains^{25, 26}.

In magnetism, noncollinear spin interactions such as DMI can trigger complex spin topologies which are incommensurate relative to the crystal structure of the host material. Such spin textures are described by multiple magnetic moment windings coexisting along multiple directions. Examples include chiral skyrmion lattices (double¹⁵ or triple²⁷ - \vec{Q}) or, the recently observed incommensurate spin crystal phases (isotropic/anisotropic double - \vec{Q})²⁸. Following the link between the topological dipole textures of ferroelectrics and ferromagnets, can this analogy be extended to multiple - \vec{Q} incommensurate polarisation textures? If possible, such a feat could hint towards the physical manifestation of an electric Dzyaloshinskii–Moriya interaction, which has recently been shown to be allowed by symmetry in ferroelectrics²⁹. In this work, we experimentally demonstrate ordered arrays of polar vortices in a single thin ferroelectric film with metallic boundary conditions. Unlike the vortex phases in $\text{PbTiO}_3/\text{SrTiO}_3$ superlattices, which show translational symmetry along the vortex core⁴, we demonstrate a new topology with an additional periodic perturbation along the vortex core, which is an analogue of the double - \vec{Q} magnetic spin crystal phase²⁸. **Motivated by the magnetic counterpart, we hypothesis either cycloidal or helical modulations as giving rise to this additional periodic perturbation. Our simulations and experimental data points towards a cycloidal winding.**

Early theoretical results have shown that closure domains are highly effective in minimizing depolarization fields in ultrathin films of BaTiO_3 (BTO) with SrRuO_3 (SRO) electrodes³⁰. We have extended these studies within the Density Functional Theory (DFT) framework and applied it to the similar PbTiO_3 (PTO)/ SrRuO_3 (SRO) system in which in-plane lattice strain is introduced through epitaxial matching to DyScO_3 (DSO). Bulk PTO has a significantly larger unit cell dipole ($\sim 90 \mu\text{C}/\text{cm}^2$) compared to BTO ($\sim 30 \mu\text{C}/\text{cm}^2$) suggesting a higher energy cost is associated with any dipole rotation. However, the polar map within the PTO layer, after relaxing the cation – oxygen octahedra, reveals a continuous rotation of the local polarization which assembles into an ordered array of polar vortices, as seen in Figure 1a. Thus, the large electrostatic energy is minimised by local rotations of surface dipoles, similar to ferromagnetic Kittel domains^{30, 31}. The DFT results suggest that this energy minimisation pathway is adopted even for metal-like boundary conditions introduced by the SRO layer which has a high charge density of $\sim 2 \times 10^{22}$ electrons/ cm^3 and a screening length of only $\sim 1 - 2 \text{ \AA}$ ³². In principle, SRO should provide better screening than SrTiO_3 , but our theoretical models reveal that it is still unable to screen the

large bound surface charges of the ferroelectric layer which forces the polarisation to develop a complex vortex array in SRO/PTO/SRO systems.

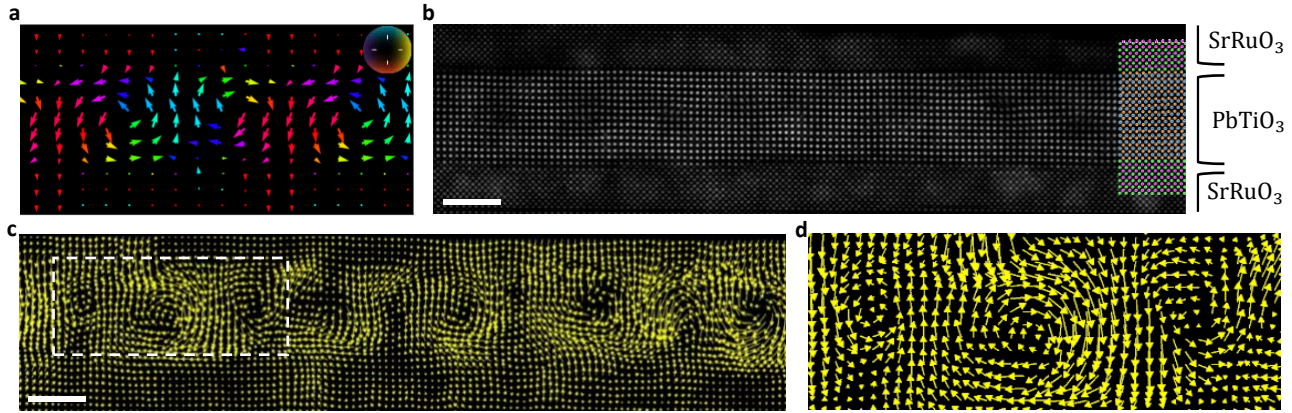


Figure 1 | Unit-cell scale electric dipole topologies. **a**, Relaxed cation – oxygen octahedra displacements map of the (SrRuO₃)_{6.5}/(PbTiO₃)_{5.5} system from DFT, where 6.5 and 5.5 refer to the number of unit cells of the respective layer. **b**, Annular Dark Field STEM (ADF-STEM) image showing the distortions within the PbTiO₃ layer. **c**, Unit cell polarization map of the ADF-STEM image revealing the local structure of the polarization pattern. **d**, Enlarged region marked by dashed lines in (c), showing the vortices formed by the polar structure. The scale bar for **b** and **c** is 2.5 nm.

Motivated by these promising DFT results showing ordered arrays of vortices in , SrRuO₃/PbTiO₃/SrRuO₃ tri-layers were grown on SrTiO₃ buffered DyScO₃ (DSO) substrates using pulsed laser deposition. The growth mode and thickness (SRO: 11 unit cells and PTO: 13 unit cells) were controlled using reflection high energy electron diffraction intensity oscillations. The topography of the top SRO layer (Extended data Figure 1a) contains step-like and atomically flat features indicating high-quality macroscopic growth. TEM studies further confirm the uniformity of the layers with sharp and abrupt interfaces between the different oxide layers (Extended data Figure 1b). Since PTO is a displacive ferroelectric, the polarization direction can be determined by knowledge of the relative positions of the B-site cations and oxygen atoms³³. Thus, the polarization can be mapped, at a unit-cell level, using aberration corrected STEM (Figure 1b). The experimentally determined polarization map reveals an ordered array of polar vortices (Figures 1c) within the ferroelectric layer. The main topological characteristics, i.e., periodicity, off-centre core, clockwise/anti-clockwise pairs, etc., are in good agreement with the DFT studies, despite the almost doubled thickness of the PTO layer in the experimental sample. The observed vortex pattern has a non-

zero toroidal moment $\mathbf{G} = (2N)^{-1} \sum_i \mathbf{r}_i \times \mathbf{P}_i$ which is parallel to the vortex core. Here \mathbf{P}_i is the local dipole moment located at \mathbf{r}_i , and N is the number of dipoles in the summation^{34, 35}. The formation of polar vortices, as highlighted in Figure 1d, in which the local dipoles rotate in such a way as to reduce both the depolarization *and* stray fields avoids the suppression of the ferroelectricity in the thin films³⁶. Furthermore, the STEM data also shows that the polarization topology is characterized by periodic pairs of clockwise (CW) – counter CW vortices, with a periodicity of about twice the thickness of the PTO film ($\sim 9\text{-}10$ nm).

Any HR-TEM analysis required to reveal domains on the nanometre level necessarily has a very limited field of view. To explore the macroscopic ordering of the polar domains more widely, we employed X-ray diffraction. The periodic structural distortions caused by the polar domains will manifest as satellite peaks in the vicinity of the layer Bragg peaks. Since these domains are within a thin PTO layer, any satellites will be extended in the reciprocal space direction normal to the substrate. Volumes of reciprocal space were mapped during scans of the sample using a two-dimensional area detector and provide simultaneous information about long-range periodic structures along all crystallographic axes. A three-dimensional reciprocal space map (RSM) was recorded in the vicinity of the $(002)_{pc}$ DSO reflections (Extended data Figure 2a), with Q_x , Q_y and Q_z co-incident with the $[h00]_{pc}$, $[0k0]_{pc}$ and $[00l]_{pc}$ directions (where pc indicates pseudocubic indices). Detailed information on the domain distribution can be obtained from the RSMs by integrating along specific crystallographic directions and reducing the data to one- or two-dimensional representations. Satellites arising from the periodic lattice distortions can be observed clearly in Figures 2a-c. Streaks of satellite intensity, centred around $Q_z = 3.1 \text{ \AA}^{-1}$ (layer Bragg peak) can be seen in the projections into the $Q_z - Q_x$ and $Q_z - Q_y$ planes (Figures 2a, b), which become clearer when projected into the $Q_x - Q_y$ plane (Figure 2c). Surprisingly, instead of only one periodicity we find a second periodicity coexisting within the PTO layer, perpendicular to the first. Along Q_x the satellites are separated by $\Delta Q_x = 0.071(1) \text{ \AA}^{-1}$ corresponding to an in-plane periodicity of $8.85(6)$ nm along the $[100]_{pc}$ direction. The periodicities in the $[010]_{pc}$ direction are less well defined, but have a separation of $\Delta Q_y = 0.078(5) \text{ \AA}^{-1}$ and hence real-space periodicities of about 8 nm. Hints of additional periodicities, also along the Q_x and Q_y directions, but with length-scales of about 20-30 nm can be seen in the tails of the central spot in the $Q_x - Q_y$ plane (Extended data Figure 3).

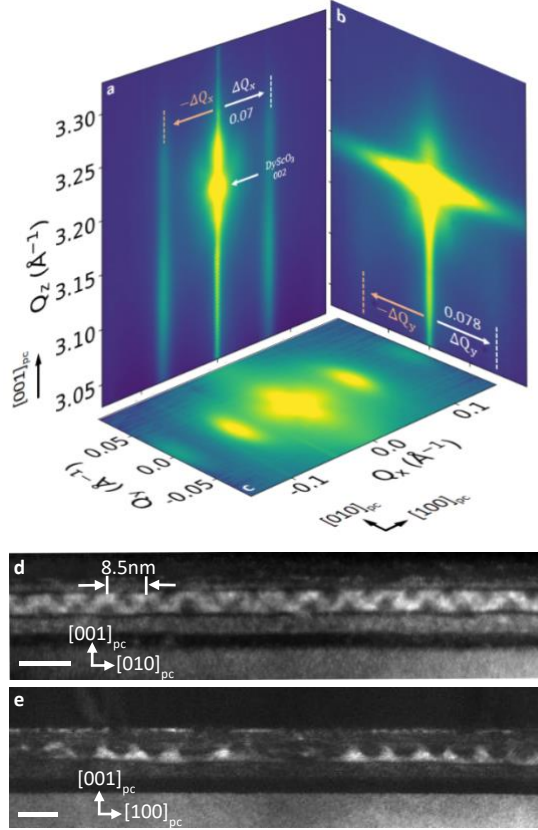


Figure 2 | Macroscopic ordering. **a**, Q_z vs Q_x reciprocal space map (RSM). **b**, Q_z vs Q_y RSM along the perpendicular direction to (a). **c**, Q_x vs Q_y RSM shows the in-plane satellite distribution corresponding to the in-plane domain patterns. **d**, Cross sectional DF-TEM close to $[100]_{pc}$ with $\mathbf{g} = 020_{pc}$ diffraction condition revealing intensity modulations with a period of about 8.5 nm. **e**, Cross sectional DF-TEM close to $[010]_{pc}$ with $\mathbf{g} = 002_{pc}$. See Extended data Figure 4 for details of the imaging conditions. The scale bars in (d) and (e) are 10 nm.

Dark field transmission electron microscopy images of the same $(010)_{pc}$ and $(100)_{pc}$ cross sections were used to reveal the real space arrangement of the PTO distortions (Figures 2d and 2e). Periodic structures can also be observed in these TEM data along both $[010]_{pc}$ and $[100]_{pc}$ directions with periodicities of about 8.5 nm and 7-10 nm, respectively which are fully consistent with the periodicities determined from the X-ray Reciprocal space maps.

Thus, regardless of the size of the probed volume, the preparation of the sample or whether the analysis was performed in real or reciprocal space, two periodic structures with similar repeat lengths of about

8.5 nm are seen simultaneously in the $[010]_{pc}$ and $[100]_{pc}$ directions. Further analysis of these periodicities was performed using plan-view TEM imaging. Dark field diffraction contrast and electron diffraction patterns, taken from thin sections of the TEM specimen, are shown in Figure 3a. The $\mathbf{g}_1 = 110_{pc}$ imaging condition reveals a labyrinthine domain structure^{37, 38} with two periodic components, running along the $[100]_{pc}$ and $[010]_{pc}$ directions. The width of the domains is about 9-10 nm and they extend for several tens of nanometres. These widths are slightly larger than the ones seen in the cross-sectional TEM and XRD which is most likely because the strain is reduced when the substrate is thinned. Selected area diffraction (SAED) patterns (upper left inset of Figure 3a) also show incommensurate satellite peaks along the $[010]_{pc}$ and $[100]_{pc}$ directions. These data are directly comparable with the macroscopic XRD data in the vicinity of the Bragg $(002)_{pc}$. The SAED patterns are highly anisotropic with satellite peaks confined to the principal axes $[h00]$ and $[0k0]$, with no scattering along other in-plane directions, in agreement with the XRD. Furthermore, images taken under two beam conditions $\mathbf{g}_2 = 100_{pc}$ and $\mathbf{g}_3 = 010_{pc}$ (Extended data Figures 5b, c) reveal the two different periodic structures independently.

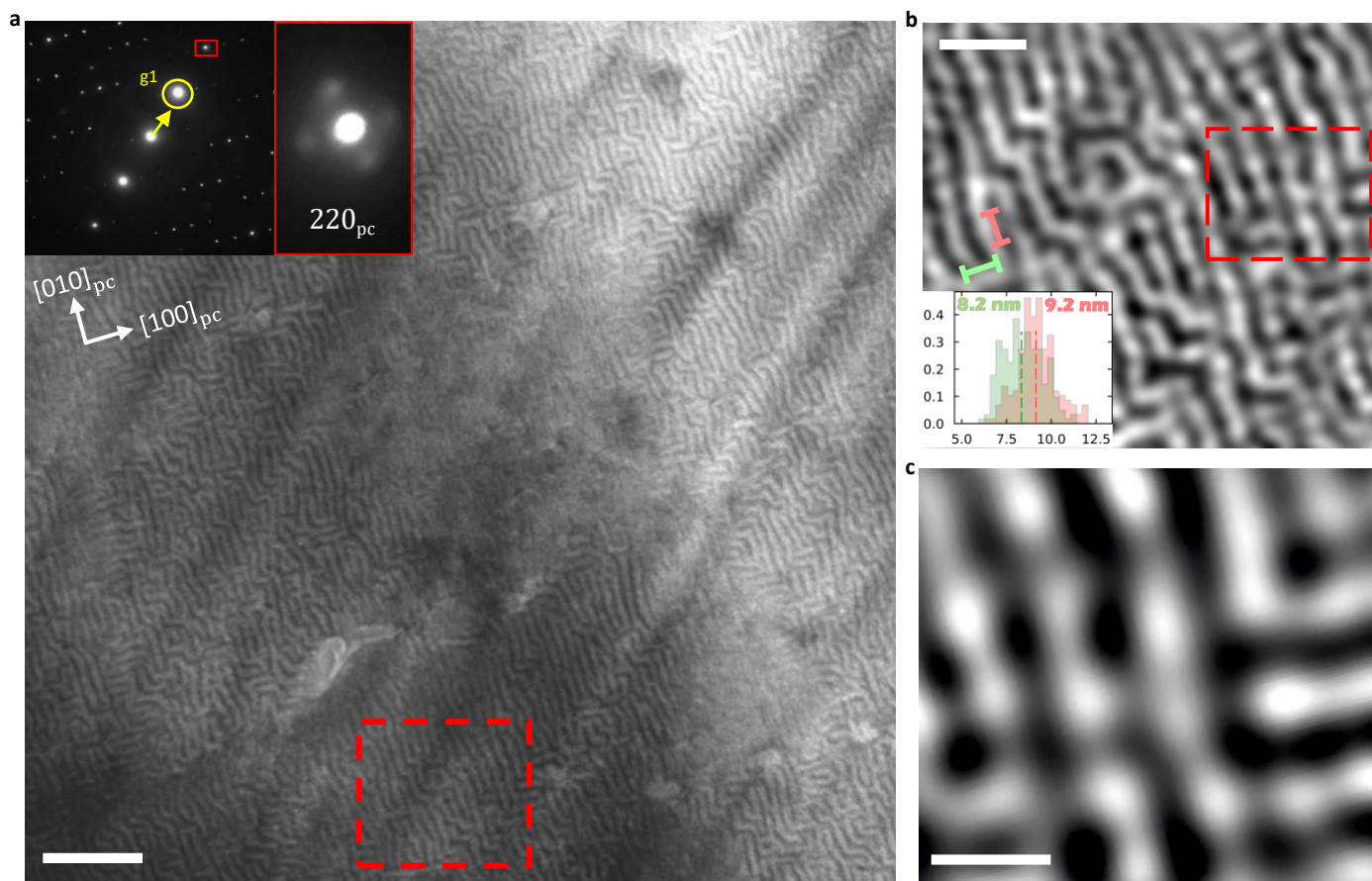


Figure 3 | Plan-view TEM imaging. **a**, Plan-view dark field TEM imaging of $(\text{SrRuO}_3)_{11}/(\text{PbTiO}_3)_{13}/(\text{SrRuO}_3)_{11}$ tri-layers which shows the intricate domain pattern formed by two coexisting periodicities along $[100]_{\text{pc}}$ and $[010]_{\text{pc}}$. The inset shows the SAED pattern with the excited $\mathbf{g}_1 = 110_{\text{pc}}$ vector. Close inspection of the diffraction spots (boxed area) reveals satellite decorations, similar to the X-ray data Q_x vs Q_y RSM. **b**, Noise filtered image showing intensity modulations *along* the individual domains. The inset graph shows the probability distribution of finding a certain modulating period of the individual domains parallel to $[100]_{\text{pc}}$ (red) and $[010]_{\text{pc}}$ (green) respectively. **c**, Magnified area shows the locally ordered modulated domains. The scale bars are: 100 nm for **a**, 30 nm for **b** and 10 nm for **c**.

The labyrinth structure imaged under the $\mathbf{g}_1 = 110_{\text{pc}}$ excitation, at first glance, appears to consist of uniform domains oriented along $[100]_{\text{pc}}$ and $[010]_{\text{pc}}$. A bandpass filter was used to improve the signal/noise ratio and enhance difficult to see features within the domains themselves (Extended data Figures 6-8). The individual domains within the labyrinth pattern contain additional periodic perturbations running along the domains. These perturbations produce modulations in the diffracted contrast intensity regardless of the domain orientation (Figure 3b). There is a slight directional dependence of the modulating period,

with the domains ordered in the $[010]_{pc}$ having periodicities of about 9.2 nm (inset Figure 3b) and those along the $[100]_{pc}$ a period of about 8.2 nm. Comparisons with the DF-TEM and X-ray data suggest that these modulations are the projection of the polar vortex array. The juxtaposition of the labyrinth and the modulations within the domains themselves generates a local rectangular lattice of alternating contrast but due to the complex domain pattern square lattice ordering is only short range (Figure 3c).

Contrast in dark field TEM images is primarily produced by the internal strain field of the vortex structures. Some insight into these strain fields can be obtained by choosing different \mathbf{g} -vectors, since the only components that contribute to contrast are parallel to \mathbf{g} . A simple two-beam Howie-Whelan simulation reproduces the essential features of the image (Extended data Figure 9). A vortex, with displacements perpendicular to its line direction \mathbf{u} , appears as a line of contrast perpendicular to \mathbf{g} and becomes invisible when \mathbf{g} is parallel to \mathbf{u} . The coexistence of two modulations is thus confirmed by the dark field $\mathbf{g} = 100_{pc}$ and $\mathbf{g} = 010_{pc}$ images, which show continuity of structures in both directions. Additionally, plan view STEM shows head-to-head and tail-to-tail polar displacements, also consistent with the second modulation having displacements along the vortex core (Extended data Figure 10).

The complex contrast texture revealed in Figure 3c shows that the domain pattern in the ferroelectric layer needs to be characterized not by one, but by two periodic components each described by a \vec{Q} vector. Thus, one \vec{Q} vector determines the periodicity of vortices, given by the alternating bright/dark segments (Extended data Figure 5c), and a second \vec{Q} vector which breaks the uniformity of the domains in the perpendicular direction, leading to a state described by a double- \vec{Q} modulation. Such incommensurate phases, triggered by multiple \vec{Q} vectors, are found in magnetic materials^{2, 27}. For example, chiral skyrmions³ are described by triple- \vec{Q} cycloidal modulations. The interplay of only two orthogonal periodic modulations results in the so-called incommensurate spin crystals^{15, 16, 28, 29}, whereby the periodicities are interwoven such that they permeate all space within the magnetic material and no region can be described by one periodicity alone. Whilst the spin crystal phases are stabilized by the non-collinear spin interactions, i.e. Dzyaloshinskii–Moriya interaction, the anisotropy energy will produce different variants of the spin crystal phase²⁸.

The possibility of an electric DM-like interaction has been put forward by Zhao et al.²⁹, where the DM energy involves trilinear couplings between oxygen octahedra and atomic displacements. For PTO, the

latter is inherently linked to its polar nature, along with its BO_6 octahedra showing no tilt. Our DFT simulations show that the PTO/SRO interface is causing the first layers of PTO to show pronounced in-phase octahedra tilts localized on the first 2 unit cells, on top of the Neel winding of the dipoles due to the vortices themselves (Extended data Figure 11). While the direction of magnetic DM vector is dictated by the crystal symmetry¹⁴, the components of the electric DM vector depend of the axes around which the oxygen cage is rotated²⁹. Tilt propagation from the SRO into the PTO could enable the oxygen octahedra rotations to couple to the Neel character of the surface dipoles resulting in DM-like interactions, as a source for the second modulation as we observe it. This interface induced effect would be analogous to the DM interaction induced by interfacial symmetry breaking in magnets^{17, 39, 40}.

Based on the TEM and XRD data presented above, we hypothesize that the ferroelectric polarisation orders itself in a domain pattern similar to the magnetic incommensurate spin crystal phases given by two perpendicular periodicities, namely the incommensurate spin crystal 1 (SC1)⁴¹.

While it is very clear that the structure that we observe has two coexisting modulation vectors, a complete model of the variation of polarisation and strain in three dimensions still remains to be determined, because we can only observe periodicities using diffraction and a projection of the structure using transmission microscopy. The plan view TEM data indicates that the weaker modulation produces periodic displacements that are parallel to the vortex core, but it remains to be determined whether this occurs by cycloidal-like modulations such as $\vec{Q}_c = C_c \sin(qx) \vec{e}_{[100]} + C_c \cos(qx) \vec{e}_{[001]}$ (x is the $\vec{e}_{[100]}$ coordinate component of the position vector), or is some other more complicated structure. For example, using our DFT to build a 3D vortex array (Figure 4a), we obtain identical plan-view projections by adding a helical-like modulation, given by $\vec{Q}_h = C_h \sin(qx) \vec{e}_{[010]} + C_h \cos(qx) \vec{e}_{[001]}$ (Figure 4b) or cycloidal-like modulation (Figure 4c). Projections of the 3D polarization model into the $[001]_{\text{pc}}-[010]_{\text{pc}}$ and $[010]_{\text{pc}}-[100]_{\text{pc}}$ planes show that both modulations preserve the vortex pattern in the cross sectional $[001]_{\text{pc}}-[010]_{\text{pc}}$ plane (Extended data Figure 12). Furthermore, the plan-view projections show a head-to-head and tail-to-tail polar topologies if the second modulation is cycloidal-like, which is consistent with the experimental plan-view STEM data (Extended data Figure 13).

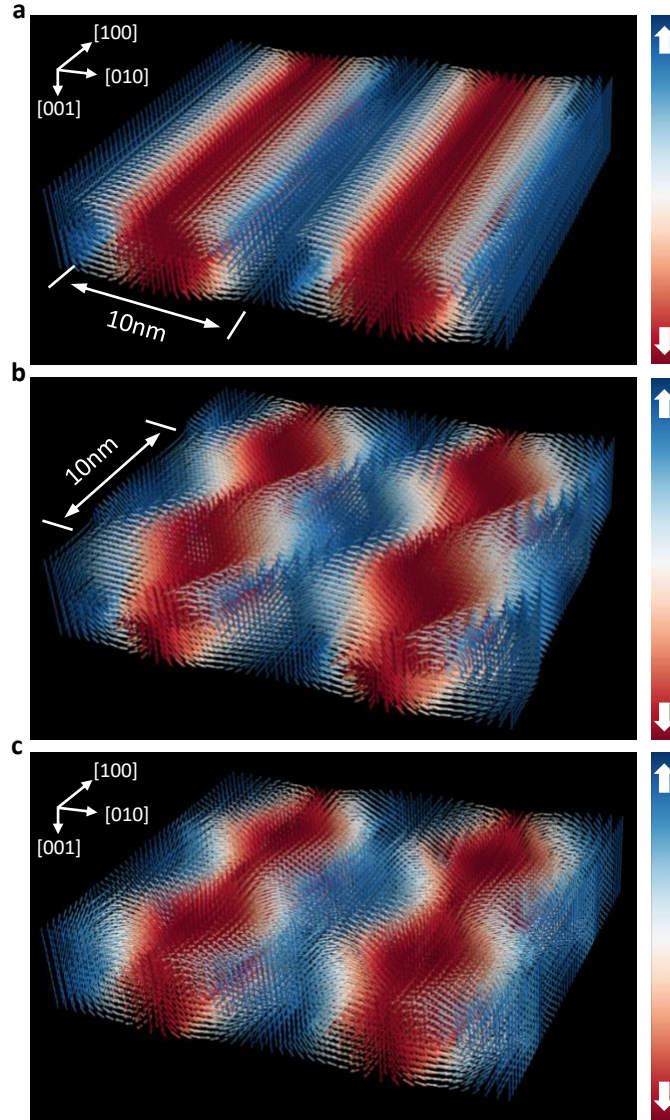


Figure 4 | Double modulation. **a**, Pseudo 3D representation showing plan and front view through a regular polar vortices. **b**, Vortex arrays with a second *helical* modulation along the vortex core. **c**, Vortex arrays with a second *cycloidal* modulation along the vortex core. The color bar maps the projection of the dipole along [001]: white regions contain dipoles oriented parallel to [010], while red and blue regions describe dipoles oriented parallel (red) and anti-parallel (blue) to [001].

Further evidence supporting the cycloidal-like interaction can be extracted from X-ray Circular Dichroism (XCD) experiments, where the helicity was reversed at each point in the scan. We used non-resonant scattering and probed the 2D topologies with the sample orientated such that either the $[100]_{pc} // [001]_o$ or the $[010]_{pc} // [-110]_o$ direction was in the scattering plane (see Extended data Figure 14). Measurement of the circular dichroism (CD) under rotation of the sample by 180° shows a weak dichroic signal when the

$[100]_{pc}$ direction is in the scattering plane, but crucially no dichroic signal upon rotating the sample by 90° (see Extended Data Figure 15). We therefore conclude that the interaction potential giving rise to the second modulation does not contain terms in \vec{Q} proportional to $\vec{e}_{[010]}$, thereby suggesting the interaction is cycloidal-like.

In summary, we have shown that ordered arrays of topological features such as polar vortices also form in a ferroelectric environment where the depolarization field is minimized by the choice of metallic SrRuO_3 electrodes. Moreover, the ferroelectric polarisation generates a new ordered phase described by a double- \vec{Q} modulation that combines a vortex state with a sinusoidal modulation. Whilst the TEM and XRD cannot distinguish between the helical and cycloidal modulations, DFT and dichroism point towards a cycloidal double- \vec{Q} structure. Such a topology mimics in detail the incommensurate spin crystal phase SC1 recently found in magnetic materials. The presence of such a double- \vec{Q} structure, mediated by incommensurate interactions, would require an electric counterpart of the magnetic DMI, which has been suggested by Zhao et al.²⁹ to be permitted by symmetry. Such an electric Dzyaloshinskii-Moriya interaction could provide the phenomenological explanation of the emergence of magnetic-like phases in ferroelectric systems. Given the similarity to the magnetic spin crystals, we chose here the simplest model to explain the data. However, we cannot rule out alternative more complex topologies that would yield similar double- \vec{Q} structures. Further advanced modelling and simulation would be necessary to identify the exact polarisation pattern they would produce and which advanced experimental methods will be needed to uniquely evidence it.

Our findings provide a potential pathway for technological exploitation and a fertile framework for further fundamental studies exploring physical phenomena. Such studies would pave the way for the exploration of complex ferroelectric topologies triggered by the electric DMI, similar to topological spin textures found in ferromagnets. Along with the discovery of polar vortices and skyrmions, our findings further blur the border between emergent ferromagnetic and ferroelectric dipole topologies. Understanding the fundamental similarities between the manifestation of spin textures across multiferroics is still lacking, however our findings provide further evidence for the potential of the ferroelectric systems to mimic their magnetic counterparts. Complex topological structures are not native to magnetism, manifesting themselves throughout the sciences⁴²⁻⁴⁴. The understanding gained from investigations of the

fundamental mechanisms within multiferroics extend far beyond applications in condensed matter physics.

References

1. Wachowiak, A. et al. Direct Observation of Internal Spin Structure of Magnetic Vortex Cores. *Science* **298**, 577-580 (2002).
2. Seki, S., Yu, X.Z., Ishiwata, S. & Tokura, Y. Observation of Skyrmions in a Multiferroic Material. *Science* **336**, 198-201 (2012).
3. Yu, X.Z. et al. Real-space observation of a two-dimensional skyrmion crystal. *Nature* **465**, 901-904 (2010).
4. Yadav, A.K. et al. Observation of polar vortices in oxide superlattices. *Nature* **530**, 198-201 (2016).
5. Hsu, S.-L. et al. Emergence of the Vortex State in Confined Ferroelectric Heterostructures. *Adv. Mater.* **31**, 1901014-1901022 (2019).
6. Shafer, P. et al. Emergent chirality in the electric polarization texture of titanate superlattices. *PNAS* **115**, 915-920 (2018).
7. Damodaran, A.R. et al. Phase coexistence and electric-field control of toroidal order in oxide superlattices. *Nature Mater* **16**, 7 (2017).
8. Stoica, V.A. et al. Optical creation of a supercrystal with three-dimensional nanoscale periodicity. *Nature Materials* **18**, 7 (2019).
9. Wang, Y.J. et al. Polar meron lattice in strained oxide ferroelectrics. *Nat. Mater.* **19**, 881-886 (2020).
10. Das, S. et al. Observation of room-temperature polar skyrmions. *Nature* **568**, 368-372 (2019).
11. Gruverman, A. et al. Vortex ferroelectric domains. *J. Phys. Condens. Matter* **20**, 4 (2008).
12. Nelson, C.T. et al. Spontaneous Vortex Nanodomain Arrays at Ferroelectric Heterointerfaces. *Nano. Lett.* **11**, 7 (2011).
13. Dzyaloshinsky, I. Thermodynamic Theory of Weak Ferromagnetism of Antiferromagnetics. *J. Phys. Chem. Solids* **4**, 241-255 (1958).
14. Moriya, T. Anisotropic Superexchange Interaction and Weak Ferromagnetism. *Phys. Rev.* **120**, 91-98 (1960).
15. Kurumaji, T. et al. Néel-Type Skyrmion Lattice in the Tetragonal Polar Magnet VOSe_2O_5 . *Phys. Rev. Lett.* **119**, 237201-237205 (2017).
16. Kurumaji, T. et al. Direct observation of cycloidal spin modulation and field-induced transition in Néel-type skyrmion-hosting VOSe_2O_5 . *Journal of the Physical Society of Japan* **90**, 024705 (2021).
17. Seddon, S.D. et al. Real-space Observation of Ferroelectrically Induced Magnetic Spin Crystal in SrRuO_3 . *Nat Commun* **12**, 2007 (2021).

18. Hong, Z. et al. Stability of Polar Vortex Lattice in Ferroelectric Superlattices. *Nano. Lett.* **17**, 7 (2017).
19. Li, X. et al. Atomic-scale observations of electrical and mechanical manipulation of topological polar flux closure. *PNAS* **117**, 18954-18961 (2020).
20. Yadav, A.K. et al. Spatially resolved steady-state negative capacitance. *Nature* **565**, 468-471 (2018).
21. Ponomareva, I., Naumov, I.I. & Bellaiche, L. Low-dimensional ferroelectrics under different electrical and mechanical boundary conditions: Atomistic simulations. *Phys. Rev. B* **72**, 5 (2005).
22. Sanchez-Santolino, G. et al. Resonant electron tunnelling assisted by charged domain walls in multiferroic tunnel junctions. *Nature Nanotech* **12**, 8 (2017).
23. Penthorn, N.E., Hao, X., Wang, Z., Hua, Y. & Jiang, H.W. Experimental Observation of Single Skyrmion Signatures in a Magnetic Tunnel Junction. *Phys. Rev. Lett.* **122**, 6 (2019).
24. Peters, J.J.P., Apachitei, G., Beanland, R., Alexe, M. & Sanchez, A.M. Polarization curling and flux closures in multiferroic tunnel junctions. *Nat Commun.* **7**, 7 (2016).
25. Hadjimichael, M. et al. Metal-ferroelectric supercrystals with periodically curved metallic layers. *Nat. Mater.* (2021).
26. Li, S. et al. Periodic arrays of flux-closure domains in ferroelectric thin films with oxide electrodes. *Appl. Phys. Lett.* **111**, 5 (2017).
27. Kurumaji, T. et al. Skyrmion lattice with a giant topological Hall effect in a frustrated triangular-lattice magnet. *Science* **365**, 914-918 (2019).
28. Yi, S.D., Onoda, S., Nagaosa, N. & Han, J.H. Skyrmions and anomalous Hall effect in a Dzyaloshinskii-Moriya spiral magnet. *Phys. Rev. B.* **80**, 054416-054421 (2009).
29. Zhao, H.J., Chen, P., Prosandeev, S., Artyukhin, S. & Bellaiche, L. Dzyaloshinskii-Moriya-like interaction in ferroelectrics and antiferroelectrics. *Nat. Mater.* **20**, 341-345 (2021).
30. Aguado-Puente, P. & Junquera, J. Ferromagnetic-like Closure Domains in Ferroelectric Ultrathin Films: First-Principles Simulations. *Phys. Rev. Lett.* **100**, 177601-177604 (2008).
31. Dürr, H.A. et al. Chiral Magnetic Domain Structures in Ultrathin FePd Films. *Science* **284**, 2166-2168 (1999).
32. Ahn, C.H. et al. Ferroelectric field effect in ultrathin SrRuO₃ films. *Appl. Phys. Lett.* **70** (1997).
33. Jia, C.-L. et al. Atomic-scale study of electric dipoles near charged and uncharged domain walls in ferroelectric films. *Nature Materials* **7** (2008).
34. Naumov, I., Bellaiche, L. & Fu, H. Unusual phase transitions in ferroelectric nanodisks and nanorods. *Nature* **432**, 4 (2004).
35. Dubovik, V.M. & Tugushev, V.V. Toroid moments in electrodynamics and solid-state physics. *Physics Reports* **187**, 57 (1990).
36. Junquera, J. & Ghosez, P. Critical thickness for ferroelectricity in perovskite ultrathin films. *Nature* **422**, 4 (2003).
37. Nahas, Y. et al. Topology and control of self-assembled domain patterns in low-dimensional ferroelectrics. *Nat Commun* **11**, 5779 (2020).
38. Nahas, Y. et al. Inverse transition of labyrinthine domain patterns in ferroelectric thin films. *Nature* **577**, 47-51 (2020).
39. Bode, M. et al. Chiral magnetic order at surfaces driven by inversion asymmetry. *Nature* **447**, 190-193 (2007).
40. Udalov, O.G., Beloborodov, I.S. & Sapozhnikov, M.V. Magnetic skyrmions and bimerons in films with anisotropic interfacial Dzyaloshinskii-Moriya interaction. *Phys Rev B* **103**, 174416 (2021).
41. Chen, J., Zhang, D.W. & Liu, J.M. Exotic skyrmion crystals in chiral magnets with compass anisotropy. *Sci. Rep.* **6**, 29126 (2016).

42. Sato, T., Ishiyama, T. & Nikuni, T. Vortex Lattice Structures of a Bose-Einstein Condensate in a Rotating Lattice Potential. *Phys Rev A* **76**, 053628 (2007).
43. Saw, T.B. et al. Topological defects in epithelia govern cell death and extrusion. *Nature* **544**, 212-216 (2017).
44. Tsesses, S. et al. Optical skyrmion lattice in evanescent electromagnetic fields. *Science* **361**, 993-996 (2018).

Methods:

Density functional Theory simulations: The calculations were performed using the Quantum Espresso suite^{45, 46} plane-wave code employing the Generalized Gradient Approximation (GGA). The exchange – correlation functional used is for solids in the Perdew-Burke-Ernzerhof parametrization⁴⁷, adapted for solids, PBEsol. We used Vanderbilt ultrasoft pseudopotentials with elements having their valence states composed of: *Pb 5d10 6s2 6p2*, *Sr 4s2 4p6 4d1 5s1 5p0*, *Ti 3s2 3p6 4s2 3d2*, *Ru 4d7 5s1 5p0*, *O 2s2 2p4*. The integration over the Brillouin zone is performed over an automatically generated Monkhorst-Pack⁴⁸ k-mesh with a Gaussian smearing of 0.01 eV. The kinetic energy cut-off is 70 Ry and 450 Ry for the charge density.

All systems have 6.5 unit-cells (uc) of SrRuO₃ and 5.5 unit-cells of PbTiO₃ (along the Z axis). In order to allow the polarization to form domains, we built a supercell with 1 uc along Y, $N_Y = 1$ and 10 uc along X, $N_X = 10$. The in-plane lattice constant is set to be equal to DyScO₃ which in the pseudocubic setting is 3.953 Å. Atomic relaxations of bulk PTO and SRO were done under the strain imposed by the substrate with the resulting unit cells used to construct the supercell. Using the PBEsol functional, the relaxed unstrained bulk PTO unit cell yield lattice constants equal to $a = 3.873(1)$ and $c = 4.218(\text{\AA})$, which results in a c/a ratio of 1.089 (within 1.7% error of the experimental value⁴⁹). The SRO layer minimum thickness was chosen such that the PTO layer was decoupled from its periodic images⁵⁰.

Spin orbit coupling is very weak for PbTiO₃ and was not considered. Hubbard corrections were not used. The supercell forces converged to less 80 meV/Å per atom (600 atoms).

Materials: We used lead titanate (PbTiO₃), strontium titanate (SrTiO₃), strontium ruthenate (SrRuO₃) and dysprosium scandate (DyScO₃). DyScO₃ is a band insulator⁵¹ with an orthorhombic unit cell belonging to the *Pbnm* space group with lattice parameters equal to $a = 5.4494 \text{ \AA}$, $b = 5.7263 \text{ \AA}$ and $c = 7.9132 \text{ \AA}$. SrTiO₃ is a band insulator⁵² with a cubic unit cell with a lattice constant $a = 3.905 \text{ \AA}$ and space group *Pm $\bar{3}$ m*. SrRuO₃ is a metal⁵³ at room temperature with a crystal symmetry which belongs to the orthorhombic Bravais lattice described by the *Pbnm* space group and lattice parameters $a = 5.5684 \text{ \AA}$, $b = 7.8425 \text{ \AA}$ and $c = 5.532 \text{ \AA}$. PbTiO₃ is a ferroelectric with a Curie temperature of 490 °C and has a tetragonal unit cell⁵⁴ described by the *P4mm* space group with $a = 3.904 \text{ \AA}$ and $c = 4.178 \text{ \AA}$.

Film growth by pulsed laser deposition: DyScO₃ (110)_o oriented substrates with a miscut angle of <0.05° were prepared by thermal annealing at 1030 °C for 2 hrs in an oxygen rich atmosphere. Epitaxial SrRuO₃/PbTiO₃/SrRuO₃ film structures were deposited onto the SrTiO₃-buffered DyScO₃ (110)_o substrates using reflective high energy electron diffraction-assisted pulsed laser deposition, which enabled precise control of the layer thickness. The thickness, growth temperature and laser fluence for STO/SRO/PTO/SRO are 10uc/11uc/13uc/11uc, 600/670/600/600 °C and ~1/0.8/1/0.8 J/cm², respectively. The laser repetition rate was 3 Hz for all layers, at 0.1 mbar oxygen pressure. The cooling rate was 20°C/min in 200 mbar of O₂. The PbTiO₃ target is an in-house compressed and sintered pellet with 10% lead excess to compensate for the high lead volatility during the layer growth at 600°C.

X-ray studies: Diffraction studies were carried out at the I16 beamline of the Diamond Light Source using an energy of 8.04 keV and a spot size of 200 µm x 60 µm [h x v]. The sample was mounted on the 6-circle kappa goniometer with a Pilatus 100K area detector and orientated using the substrate reflections to ensure precise crystallographic projections were recorded and high-quality 3D Reciprocal Space Maps produced. For simplicity we refer to the planes and directions in the pseudo-cubic setting which have the following epitaxial relationships: [110]_o = [001]_{pc}; [001]_o = [100]_{pc}; [-110]_o = [010]_{pc}. Dichroism experiments were performed at 7.7 keV on beamline 4-ID-D at the Advanced Light Source, Argonne National Laboratory with the circular polarised light generated using a diamond phase retarder. Lab based XRD studies were also performed using a Panalytical X'Pert Pro MRD diffractometer with Cu K_α radiation and an 1D PiXcel detector.

Sample preparation for Electron Microscopy studies: STEM and cross-sectional DF-TEM samples were prepared using the TESCAN FIB-SEM system. The sample was flat-polished starting with an ion energy of 30 keV before decreasing down to 2 keV for the final polish. Plan-view DF-TEM samples were flat polished on an Allied High Tech Multiprep down to 30 µm followed by further thinning in a Gatan Precision Ion Polishing System with a starting energy of 6 keV which decreased to 100 eV for final cleaning. STEM images were recorded in a double CEOS-corrected Schottky emission JEOL ARM-200F microscope operating at 200 kV. Annular Dark Field signals were collected in the range between 45–180 mrad, with a probe forming a convergence semi-angle of 21 mrad. For accurate position/displacement measurements, each image is reconstructed from several orthogonal fast scans which were aligned for rigid and non-rigid distortions using the SmartAlign routines⁵⁵. Atomic positions were then found using nonlinear least squares fitting of 2D Gaussian functions including contributions from nearest neighbours. Diffraction

contrast images were recorded with two beam conditions on a JEOL 2100 with a LaB₆ filament operating at 200 kV.

Methods References:

45. Giannozzi, P. et al. Advanced capabilities for materials modelling with quantum espresso. *Journal of Physics: Condensed Matter* (2017).
46. Giannozzi, P. et al. Quantum espresso: a modular and open-source software project for quantum simulations of materials. *Journal of Physics: Condensed Matter*, 19 (2009).
47. Perdew, J.P., Burke, K. & Ernzerhof, M. Generalized gradient approximation made simple. *Phys. Rev. Lett.* **77** (1996).
48. Monkhorst, H.J. & Pack, J.D. Special points for brillouin-zone integrations. *Phys. Rev. B* **13** (1976).
49. Zhang, Y., Sun, J., Perdew, J.P. & Wu, X. Comparative first-principles studies of prototypical ferroelectric materials by LDA, GGA, and SCAN meta-GGA. *Phys. Rev. B.* **96** (2017).
50. Kolpak, A.M., Sai, N. & Rappe, A. Short-circuit boundary conditions in ferroelectric PbTiO₃ thin films. *Phys. Rev. B* **74**, 054112-054117 (2006).
51. Leferovich, R.P. & Mitchell, R.H. A structural study of ternary lanthanide orthoscandate perovskites. *Journal of Solid State Chemistry* **177**, 2188-2197 (2004).
52. Longo, V.M. et al. On the photoluminescence behavior of samarium-doped strontium titanate nanostructures under UV light. A structural and electronic understanding. *Phys. Chem. Chem. Phys.* **12**, 7566-7579 (2010).
53. Bansal, C., Kawanaka, H., Takahashi, R. & Nishihara, Y. Metal–insulator transition in Fe-substituted SrRuO₃ bad metal system. *Journal of Alloys and Compounds* **360**, 47-53s (2003).
54. Kuroiwa, Y., Aoyagi, S. & Sawada, A. Evidence for Pb-O Covalency in Tetragonal PbTiO₃. *Phys Rev Lett* **87**, 217601-217605 (2001).
55. Jones, L. et al. Smart Align—a new tool for robust non-rigid registration of scanning microscope data. *Adv Struct Chem Imag* **1** (2015).

Acknowledgements:

The work was partly supported by the EPSRC (UK) through grants no. EP/P031544/1 and EP/P025803/1. M.A. acknowledges the Theo Murphy Blue-sky Award of Royal Society. This research used resources of the Advanced Photon Source, a U.S. Department of Energy (DOE) Office of Science User Facility, operated for the DOE Office of Science by Argonne National Laboratory under Contract No. DE-AC02-06CH11357. The authors also acknowledge the technical support from Mr. Michael Crosbie. The authors would like to acknowledge the University of Warwick Research Technology Platform for assistance in the research described in the current paper.

Author Contributions:

MA conceived the idea. DR, MA and AMS designed the experiments. DR prepared the samples, performed DFT and DF-TEM experiments and analysed the data. JJPP and JAG performed the STEM experiments and analysis. GN, JS, DH and DR collected the synchrotron data. TPAH and DR analysed the XRD data. RB performed the 2-beam diffraction contrast simulations. All authors contributed to the discussions. All authors wrote the manuscript.

Competing Interests: The authors declare no competing interests.

Additional information

Correspondence and requests for materials should be addressed to M.A.